

Whole-Body Integrated Motion Planning for Aerial Manipulators

Weiliang Deng^{1*}, Hongming Chen^{1*}, Biyu Ye¹, Haoran Chen¹ and Ximin Lyu^{1†}

Abstract—Efficient motion planning for Aerial Manipulators (AMs) is essential for tackling complex manipulation tasks, yet achieving coupled trajectory planning remains challenging. In this work, we propose, to the best of our knowledge, the first whole-body integrated motion planning framework for aerial manipulators, which is facilitated by an improved Safe Flight Corridor (SFC) generation strategy and high-dimensional collision-free trajectory planning. In particular, we formulate an optimization problem to generate feasible trajectories for both the quadrotor and manipulator while ensuring collision avoidance, dynamic feasibility, kinematic feasibility, and waypoint constraints. To achieve collision avoidance, we introduce a variable geometry approximation method, which dynamically models the changing collision volume induced by different manipulator configurations. Moreover, waypoint constraints in our framework are defined in $SE(3) \times \mathbb{R}^3$, allowing the aerial manipulator to traverse specified positions while maintaining desired attitudes and end-effector states. The effectiveness of our framework is validated through comprehensive simulations and real-world experiments across various environments.

Index Terms—Aerial manipulator, delta arm, motion planning, collision avoidance, waypoint constraint.

I. INTRODUCTION

AERIAL manipulators, which consist of Unmanned Aerial Vehicles (UAVs) and manipulators, have garnered significant interest from researchers and industries due to their wide operational range and agile manipulation capabilities [1]. These systems have proven to operate effectively in challenging or hazardous environments, facilitating applications across various fields such as 3D printing, inspection, transportation, grasping, and perching. [2]–[5].

Various aspects of aerial manipulators have been extensively studied, including platform design [6], [7], motion planning [8], [9], and precise control [10]–[12]. Despite these advancements, a notable gap persists in the realm of coupled planning frameworks capable of synchronizing UAV and manipulator motions to unleash the full potential of the system. Unlike decoupled approaches that separately plan the UAV and manipulator trajectories, coupled planning enables coordinated motion generation for the entire system, preserving its full maneuverability for complex tasks [13]. In developing coupled planning frameworks, collision avoidance emerges as a key requirement, as it ensures safe interaction with environments. This capability forms the foundation for high-level operations such as pick-and-place tasks [8] and enhances adaptability

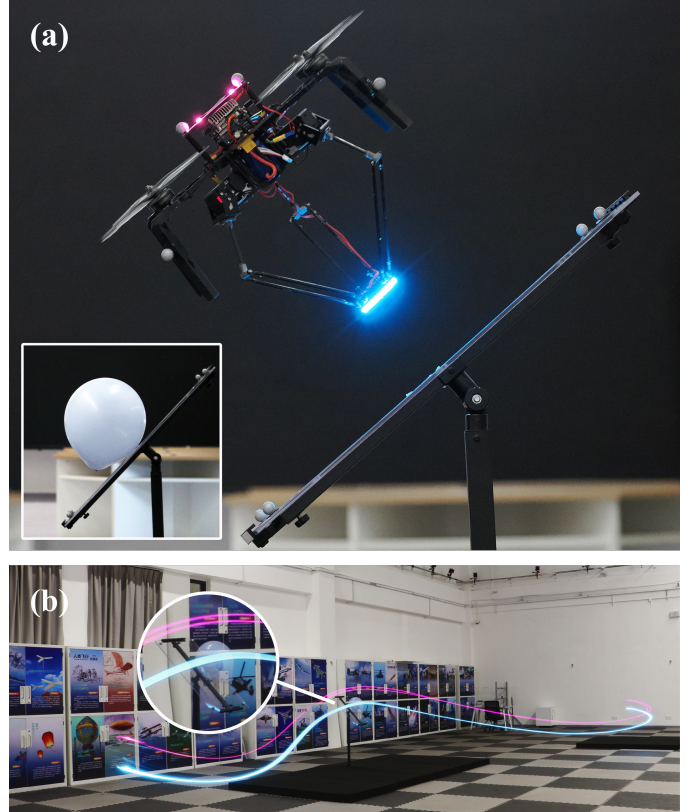


Fig. 1. Demonstration of whole-body integrated motion planning for an aerial manipulator performing a precision task. (a) The aerial manipulator executes a planned trajectory to reach a specified waypoint, maintaining an attitude parallel to the inclined plane while configuring its delta arm for balloon piercing. (b) Time-lapse visualization capturing the complete execution of the planned motion. The experiment video is available at <https://youtu.be/gK9XuNWhxKg>.

across diverse scenarios. Moreover, beyond collision avoidance, numerous aerial manipulation activities such as perching, grasping, and striking, require high-order waypoint constraints that specify velocities or attitudes at critical points. For example, aerial manipulators must maintain specific attitudes at certain positions to achieve manipulation on inclined surfaces, as illustrated in Figure 1. By incorporating these high-order waypoint constraints, our proposed framework enables aerial manipulators to execute a diverse range of manipulation tasks with enhanced reliability.

Coupled planning for aerial manipulators presents significant challenges, with the most fundamental stemming from the high-dimensional state space. The inclusion of additional joints from the manipulators greatly increases the system's

* Equal contribution. † Corresponding Author.

¹ School of Intelligent Systems Engineering, Sun Yat-sen University, Shenzhen, 528406, China. Emails: {dengwliang, chenhm223, yeby9, chenhr66}@mail2.sysu.edu.cn, lvxm6@mail.sysu.cn

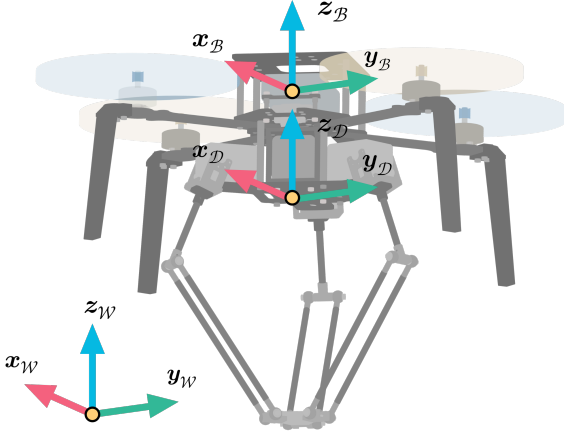


Fig. 2. Coordinate frames of the aerial manipulator system: World frame (\mathcal{F}_W), Body frame (\mathcal{F}_B), and Delta frame (\mathcal{F}_D).

dimensionality, resulting in a vastly expanded search space. To address the challenges of high-dimensional motion planning, various approaches have been developed. These methods are generally classified into two main categories: learning-based methods and optimization-based methods. Learning-based methods, particularly Reinforcement Learning (RL), have shown promising results in aerial manipulation. Previous work has demonstrated that RL can handle motion planning strategies for challenging tasks like door opening without requiring an accurate analytical model [14]. Similarly, recent research has employed model-based Deep Reinforcement Learning (DRL) to learn policies for environmental interactions, such as pushing objects on a surface to goal points [15]. However, these methods rely heavily on simulation for training and may have limited generalization capabilities when encountering novel scenarios not seen during training. Optimization-based methods, on the other hand, can provide high-quality, natural, and efficient solutions by solving objective functions. Early work proposes an optimization-based framework for aerial manipulators, focusing on aerial grasping of moving targets [16]. However, this approach primarily prioritized time minimization while overlooking other critical performance metrics, such as energy consumption. More recently, researchers develop a discrete-mechanics-based time-optimal trajectory planning framework for aerial manipulators with complementarity constraints [4]. Despite its advancements, this method is limited in its applicability to high-attitude manipulation scenarios.

For collision avoidance, the primary challenge for aerial manipulators lies in handling their varying configurations during manipulation tasks. Specifically, the manipulator's extended configuration substantially increases the overall collision volume compared to its retracted state. This dynamic change in collision volume adds significant complexity, particularly in cluttered environments. Early research attempts to address this challenge by simplifying the environment to reduce the risk of potential collisions [16], [17]. However, this strict

reliance on simplified environments severely limits practical applications. Later approaches address the issue by treating the system as a conventional quadrotor, retracting the manipulator during flight and extending it upon reaching the target [8], [18]. This strategy allows for the straightforward application of existing collision avoidance methods designed for quadrotors. However, such a multi-stage approach overlooks the dynamic interactions between the UAV and the manipulator, leading to uncoordinated performance and a significant reduction in overall efficiency [19]. An alternative perspective approximates the collision volume of aerial manipulators using simple geometric models to enable efficient collision avoidance computation. Early approximation methods focus on quadrotors, using constant ellipsoids to represent their collision volume [20]. To enable more agile and aggressive flight, researchers develop compact polyhedron models [21]. However, applying these approximation methods to aerial manipulators presents significant challenges. The core issue lies in balancing safety and performance: conservative geometric bounds ensure collision avoidance but severely restrict agility, whereas tighter approximations allow for more dynamic and agile motion but increase the risk of collisions in complex environments.

Waypoint constraints play a critical role in task execution for aerial manipulators, yet they pose significant challenges due to the need to satisfy precise intermediate-state requirements while maintaining feasibility across the entire trajectory. Existing methods for handling waypoint constraints fall into two main categories: multi-stage planning and optimization integration methods. In multi-stage planning, the trajectory is divided into segments by setting multiple start and goal points [22]. While this approach can simplify the planning process, it struggles to handle higher-order constraints at key waypoints. For optimization integration methods, two primary strategies are employed: penalizing deviations from specific waypoints [23], [24] or treating waypoints as equality constraints [25]. The penalty-based strategy provides flexibility in trajectory generation but faces challenges in balancing waypoint penalties with other objective terms, and the equality constraint strategy severely guarantees waypoint satisfaction but introduces additional computational burden.

A particular type of higher-order waypoint constraint for aerial manipulators involves attitude constraints, which are challenging to address due to quadrotors' inherent underactuation [26]. Researchers have proposed various solutions to address attitude constraints. One method involves developing fully actuated UAVs [26], [27] that use multiple inclined propellers to achieve complete 6-dimensional pose control. However, these designs require specialized hardware configurations that deviate from commercially available UAVs, limiting their widespread adoption. An alternative method leverages multiple UAVs as distributed thrust generators to achieve full actuation, as demonstrated by the Spherically connected MultiQuadrotor (SmQ) platform [28]. However, this approach introduces increased system complexity, potentially leading to decreased robustness and greater uncertainty [27].

In this paper, we propose a whole-body integrated planning framework for aerial manipulators that focuses on collision avoidance under various manipulator configurations while in-

corporating $SE(3) \times \mathbb{R}^3$ waypoint constraints. First, we develop an improved SFC generation strategy that expands the feasible solution space. Second, we decompose the waypoint constraints into \mathbb{R}^6 and $SO(3)$ components. We implement the \mathbb{R}^6 waypoint constraints through a spatial-temporal decomposition trajectory representation [29], which strategically partitions spatial information into optimization variables and constant parameters. Third, we formulate an optimization problem to generate a 6-dimensional trajectory, which includes the quadrotor's trajectory in the world frame and the manipulator's trajectory in the local frame. This optimization incorporates penalty terms for safety, dynamic feasibility, kinematic feasibility, and high-order waypoint constraints. For safety considerations, we introduce a novel dynamic ellipsoidal approximation to model the aerial manipulator's collision volume. The shape of the approximation model directly depends on the end-effector state. To handle $SO(3)$ waypoint constraints, we apply an attitude penalty at specific points using a relaxation function [30]. This approach, combined with our \mathbb{R}^6 components, enables the full implementation of constraints in $SE(3) \times \mathbb{R}^3$. Ultimately, we validate our framework through extensive simulations and real-world experiments across diverse environments. The main contributions of this work are:

- 1) **Whole-body Planning Framework:** As far as we know, we propose the first whole-body integrated motion planning framework for aerial manipulators. This framework simultaneously optimizes the trajectory of both the quadrotor and the manipulator, ensuring safety, dynamic and kinematic feasibility, as well as waypoint constraints.
- 2) **Dynamic Approximation:** To address whole-body collision avoidance, we employ a dynamic ellipsoidal approximation for collision modeling. This approach ensures collision-free trajectories by accounting for varying manipulator configurations in obstacle-rich environments.
- 3) **$SE(3) \times \mathbb{R}^3$ Waypoint Constraints:** We propose a method to handle $SE(3) \times \mathbb{R}^3$ waypoint constraints. This method ensures that the aerial manipulator satisfies both attitude constraints and end-effector state constraints when passing through specific points.
- 4) **Validation and Open Source:** We demonstrate the effectiveness and applicability of our approach through comprehensive simulations and real-world experiments. The code will be made publicly available to benefit the research community <https://github.com/SYSU-HILAB/am-planner.git>.

Our framework overview is depicted in Figure 3. The paper is organized as follows. Section II introduces the notation, system model, and trajectory representation. Section III presents the improved SFC generation strategy, while Section IV elaborates on the optimization framework. Section V validates the effectiveness of the proposed method through simulations and experiments. Finally, conclusions are presented in Section VI.

II. PRELIMINARIES

A. Notation

The aerial manipulator discussed in this paper comprises a quadrotor and a delta arm, as shown in Figure 2. According to [31], the customized manipulator constitutes only a small fraction of the total mass of the entire aerial manipulator system. Therefore, it is reasonable to assume that the Center of Mass (CoM) of the quadrotor coincides with the CoM of the entire aerial manipulator. To accurately model the system's dynamics, we define three distinct coordinate frames:

- 1) **World Frame (\mathcal{F}_W):** This frame is denoted by $\{\mathbf{x}_W, \mathbf{y}_W, \mathbf{z}_W\}$, where \mathbf{z}_W points upwards, opposing the direction of gravity.
- 2) **Body Frame (\mathcal{F}_B):** This frame is represented by $\{\mathbf{x}_B, \mathbf{y}_B, \mathbf{z}_B\}$. The origin of this frame is located at the CoM of the aerial manipulator. In this frame, \mathbf{x}_B points forward and \mathbf{z}_B aligns with the total thrust generated by the rotors.
- 3) **Delta Frame (\mathcal{F}_D):** This frame is specified as $\{\mathbf{x}_D, \mathbf{y}_D, \mathbf{z}_D\}$ and is related to the body frame \mathcal{F}_B through a translational transformation only.

Unless explicitly stated otherwise, the pre-superscript of a vector indicates the frame in which the vector is expressed. For conciseness, when a vector is expressed in the world frame, the pre-superscript will be omitted. For instance, \mathbf{p}_b represents the position of the CoM of the aerial manipulator, in \mathcal{F}_W , while ${}^D\mathbf{p}_e$ denotes the position of the end effector in \mathcal{F}_D . Analogously, the matrix \mathbf{R}_B represents the rotation from \mathcal{F}_W to \mathcal{F}_B .

Let $\mathbf{p}_o = [\mathbf{p}_{b,o}^\top, {}^D\mathbf{p}_{e,o}^\top]^\top \in \mathbb{R}^6$ and $\mathbf{p}_f = [\mathbf{p}_{b,f}^\top, {}^D\mathbf{p}_{e,f}^\top]^\top \in \mathbb{R}^6$ denote the origin and final positions of the aerial manipulator in \mathcal{F}_W and end effector in \mathcal{F}_D , respectively. Similarly, let $\mathbf{p}_\lambda^{\text{sp}} = [\mathbf{p}_{b,\lambda}^{\text{sp}\top}, {}^D\mathbf{p}_{e,\lambda}^{\text{sp}\top}]^\top \in \mathbb{R}^6$ and $\mathbf{n}_{b,\lambda}^{\text{sp}} \in \mathbb{R}^3$ ($\lambda \in \{1, 2, \dots, n_\Lambda\}$) denote the specific waypoint positions and corresponding orientations, where $\mathbf{p}_{b,\lambda}^{\text{sp}}$ and ${}^D\mathbf{p}_{e,\lambda}^{\text{sp}}$ are λ -th waypoint for the aerial manipulator in \mathcal{F}_W and end effector in \mathcal{F}_D . Here, ${}^D\mathbf{p}_{e,\lambda}^{\text{sp}}$ must lie within the workspace of the delta arm.

B. Dynamic Model

The aerial manipulator in this paper consists of 9 Degrees of Freedom (DoFs), with the quadrotor providing 6 DoFs and the delta arm contributing 3 translational DoFs. This configuration enhances maneuverability and agility in various tasks but also increases planning complexity in the high-dimensional space.

Previous research [25] leverages the differential flatness of the multirotor and design a robust controller for the entire system to effectively reject the inertial effects induced by the manipulator. Similarly, a previous work [31] proposes a controller that compensates for the coupled dynamics between the quadrotor and the delta arm, enabling independent trajectory tracking for both subsystems. Inspired by these works, we preserve the differential flatness property of the quadrotor and employ a similar controller to compensate for the coupled dynamics. Specifically, we first analyze the dynamics of the

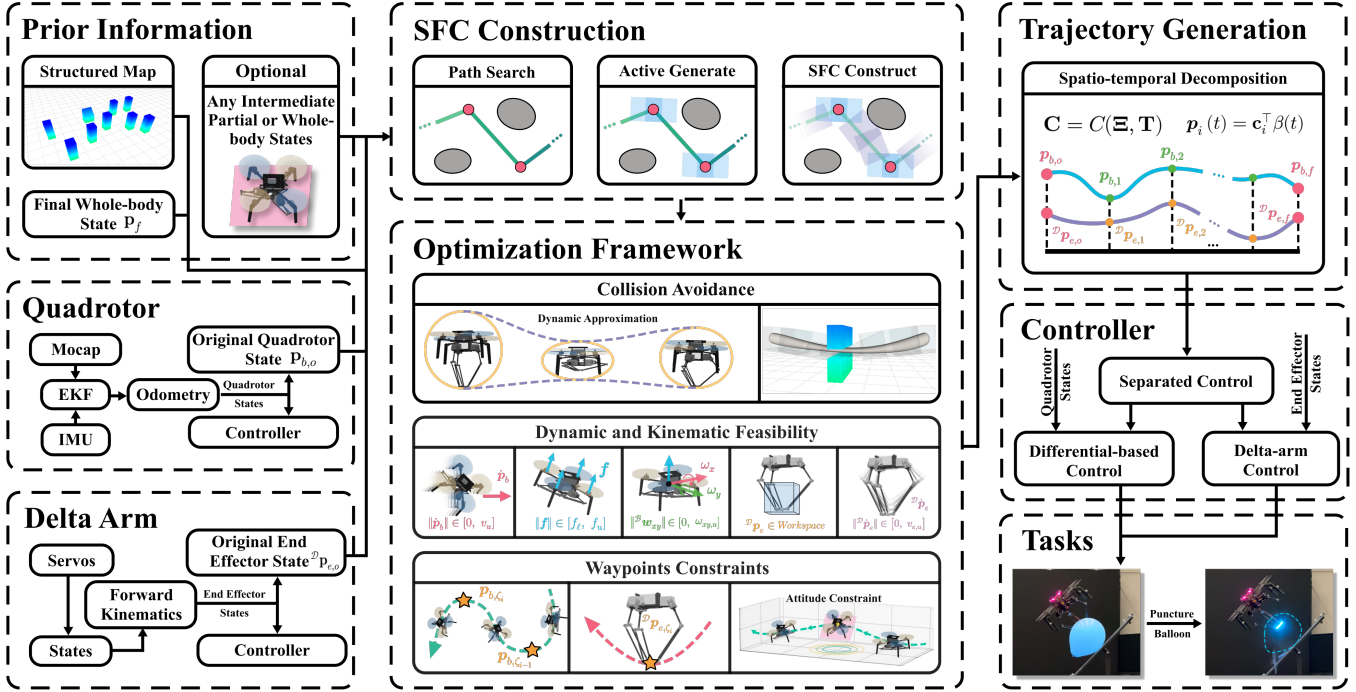


Fig. 3. Overview of our proposed integrated motion planning framework. The framework comprises seven components: (a) Prior Information module processing user-defined inputs (structured map data, final whole-body states, and optional task-specific requirements); (b) Quadrotor module integrating Mocap, EKF, and IMU for state estimation; (c) Delta Arm module handling servo control and forward kinematics for Cartesian space state computation; (d) SFC Construction module for path searching, active polyhedrons generation and conventional SFC construction; (e) Optimization Framework addressing collision avoidance, dynamic and kinematic feasibility, and waypoint constraints; (f) Trajectory Generation module for polynomial trajectories; and (g) Control component implementing separated control strategy. The framework's effectiveness is validated through balloon puncture experiments.

quadrotor and the delta arm separately, and then combine them into the whole-body dynamics of the aerial manipulator.

1) **Quadrotor Dynamics:** According to [31], the modified normalized thrust \hat{f} and the modified torque $\hat{\tau}$ are expressed as:

$$\hat{f} = f + f^d, \quad (1)$$

$$\hat{\tau} = \tau + \tau^d. \quad (2)$$

Here, $f = fz_B \in \mathbb{R}^3$ and $\tau \in \mathbb{R}^3$ represent the total normalized thrust along z_B and the total torque generated by the rotors, respectively. The scalar f denotes the magnitude of the total thrust. The vectors $f^d \in \mathbb{R}^3$ and $\tau^d \in \mathbb{R}^3$ correspond to the disturbance forces and torques caused by coupled dynamics, respectively. However, since these disturbances can be largely compensated by the control strategy, we assume $f^d \approx 0$ and $\tau^d \approx 0$ during the planning phase.

Based on the summary above, the dynamics of the quadrotor can be represented as:

$$\hat{f} = \ddot{p}_b + gz_{\mathcal{W}}, \quad (3)$$

$$\hat{\tau} = \mathcal{I} \cdot {}^B \dot{\omega}_b + {}^B \omega_b \times (\mathcal{I} \cdot {}^B \omega_b) \quad (4)$$

where $\ddot{p}_b \in \mathbb{R}^3$ is the acceleration, $g \in \mathbb{R}^+$ denotes the magnitude of gravitational acceleration. $\mathcal{I} \in \mathbb{R}^{3 \times 3}$ represents the moment of inertia matrix, ${}^B \omega_b \in \mathbb{R}^3$ is the angular velocity vector in \mathcal{F}_B , and ${}^B \dot{\omega}_b \in \mathbb{R}^3$ is its time derivative.

By leveraging the differential flatness property demonstrated in [32], the complete state of the quadrotor, defined as

$$x_b(t) := [p_b, \mathbf{R}_B, \dot{p}_b, {}^B \omega_b], \quad (5)$$

can be fully expressed in terms of the flat output:

$$y_b(t) := [p_b, \psi]. \quad (6)$$

2) **Delta-arm Dynamics:** Given that our planning framework is solved within Cartesian space, it is imperative to leverage Inverse Kinematics (IK) to construct the mapping between the position ${}^D p_e$ and the joint angles $q = [q_1, q_2, q_3]^T \in \mathbb{R}^3$. Let $L_u, L_l \in \mathbb{R}$ denote the lengths of the upper arm and lower arm, respectively. The circumradius of the static platform is denoted by $r_s \in \mathbb{R}$, and the circumradius of the end effector is denoted by $r_d \in \mathbb{R}$.

Leveraging the methodology delineated in [33], the relationship between the position of the end effector in the delta frame ${}^D p_e$ and the joint angles q can be obtained by solving the following equation :

$$\left\| {}^D p_e - {}^D \mathbf{R}_i \cdot \begin{bmatrix} r_s + L_u \sin q_i \\ 0 \\ -L_u \cos q_i \end{bmatrix} \right\|_2 = L_l^2, \quad (7)$$

where $i \in \{1, 2, 3\}$, and ${}^D \mathbf{R}_i$ denotes the z -axis rotation matrix by $\{0, \frac{2}{3}\pi, \frac{4}{3}\pi\}$ radians, respectively.

Differentiating the both sides of the above equation with respect to time and rearranging the terms yields:

$$\dot{q} = \mathbf{J}^D \dot{p}_e, \quad (8)$$

where \mathbf{J} denotes the Jacobian matrix with its explicit expression given in [31].

3) **Whole-body Dynamics:** Building upon the decoupled analysis, we integrate the system dynamics to leverage their advantages in trajectory generation [34]. For the aerial manipulator system, we establish differential flatness through a carefully selected set of variables [25], defining the flat output $\mathbf{y}(t)$ as:

$$\mathbf{y}(t) := [\mathbf{p}_b, \psi, \mathcal{D}\mathbf{p}_e]. \quad (9)$$

Consider the whole state of an aerial manipulator system with a delta arm:

$$\mathbf{x}(t) := [\mathbf{p}_b, \mathbf{R}_B, \dot{\mathbf{p}}_b, {}^B\boldsymbol{\omega}_b, \mathbf{q}] \quad (10)$$

and the control input is defined as:

$$\mathbf{u}(t) := [\mathbf{f}, \boldsymbol{\tau}, \dot{\mathbf{q}}]. \quad (11)$$

According to the above dynamics of the quadrotor and the delta arm, we can easily find that the state $\mathbf{x}(t)$ and input $\mathbf{u}(t)$ can be expressed as functions of the flat output $\mathbf{y}(t)$ and its derivatives:

$$\mathbf{x}(t) = \Psi_x(\mathbf{y}, \mathbf{y}^{(1)}, \mathbf{y}^{(2)}, \mathbf{y}^{(3)}; t); \quad (12)$$

$$\mathbf{u}(t) = \Psi_u(\mathbf{y}, \mathbf{y}^{(1)}, \mathbf{y}^{(2)}, \mathbf{y}^{(3)}, \mathbf{y}^{(4)}; t), \quad (13)$$

where Ψ_x and Ψ_u are mapping functions from the \mathbf{y} and its finite derivatives $\mathbf{y}^{(n)}$ to the state $\mathbf{x}(t)$ and input $\mathbf{u}(t)$, respectively. Thus, to summarize, based on the aforementioned assumptions, Equation (9), Equation (12), and Equation (13) collectively confirm that the equations of motion for the aerial manipulator are differentially flat with respect to the flat outputs $\mathbf{y}(t)$.

C. Trajectory Representation

In this study, we employ the segmental polynomial trajectories, i.e. MINCO [29], to perform spatio-temporal decomposition, leveraging the differential flatness properties:

$$\mathfrak{T}_{\text{MINCO}} = \{\mathbf{p}(t) : [0, T_\sigma] \mapsto \mathbb{R}^m \mid \mathbf{C} = C(\mathbf{q}, \mathbf{T})\} \quad (14)$$

where m represents the dimension of the trajectory. In this study, we omit yaw angle planning (set to zero for simplicity) and focus on generating 6-dimensional trajectories, i.e., $m = 6$. $\mathbf{C} = [\mathbf{c}_1^\top, \dots, \mathbf{c}_M^\top]^\top \in \mathbb{R}^{2Ms \times m}$ denotes the polynomial coefficient matrix, where M represents the number of segments in the polynomial trajectory and s represents the order of the integrator chain for control effort. $\mathbf{q} = [\mathbf{q}_1, \dots, \mathbf{q}_{M-1}]^\top \in \mathbb{R}^{(M-1) \times m}$ represents the intermediate points, and $\mathbf{T} = [T_1, \dots, T_M]^\top \in \mathbb{R}_{>0}^M$ represents the non-negative time vector. $C(\mathbf{q}, \mathbf{T})$ denote the parameter mapping constructed from Theorem 2 in [29], and $T_\sigma = \sum_{i=1}^M T_i$ is the sum of time.

For the i -th segment of the trajectory, $\mathbf{p}_i(t)$ is defined as:

$$\mathbf{p}_i(t) = \mathbf{c}_i^\top \boldsymbol{\beta}(t), \quad t \in [0, T_i], \quad (15)$$

where $i \in \{1, 2, \dots, M\}$, and T_i represents the duration of the i -th segment. The polynomial coefficient matrix for the i -th segment is denoted by $\mathbf{c}_i \in \mathbb{R}^{2s \times m}$, and the basis vector function $\boldsymbol{\beta}(x)$ is defined as $\boldsymbol{\beta}(x) = [1, x, \dots, x^{2s-1}]^\top \in \mathbb{R}^{2s}$.

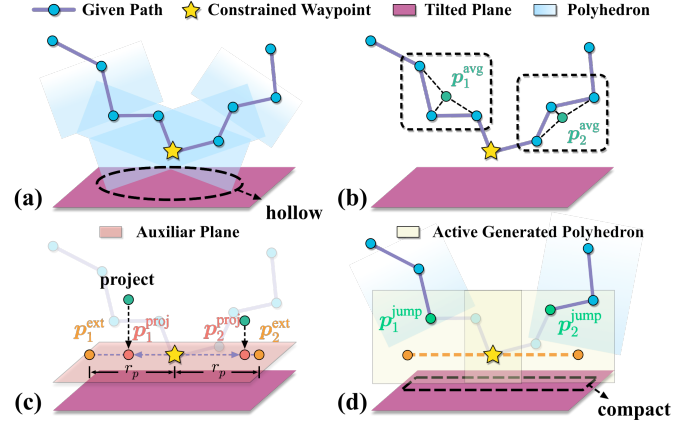


Fig. 4. Active polyhedrons generation algorithm: (a) hollow spaces from SFC generation on inclined surfaces; (b) computation of averaged points $\mathbf{p}_1^{\text{avg}}$ and $\mathbf{p}_2^{\text{avg}}$ from path points; (c) projection onto auxiliary planes yielding $\mathbf{p}_1^{\text{proj}}$, $\mathbf{p}_2^{\text{proj}}$ and extensions $\mathbf{p}_1^{\text{ext}}$, $\mathbf{p}_2^{\text{ext}}$; (d) polyhedron generation using constrained waypoints with points $\mathbf{p}_1^{\text{ext}}$ and $\mathbf{p}_2^{\text{ext}}$ for compact adherence to the surface.

III. ACTIVE SFC GENERATION

Given the specific waypoint positions $\mathbf{p}_{b,\lambda}^{\text{sp}}$ and orientations $\mathbf{n}_{b,\lambda}^{\text{sp}} (\lambda \in \{1, 2, \dots, n_\Lambda\})$, our objective is to generate a safe and feasible trajectory for the aerial manipulator while satisfying all the waypoint constraints. To achieve this objective, we propose a modified SFC generation strategy that combines multi-stage path searching with an active polyhedrons generation method at specific points which not only enables waypoint constraint implementation but also enlarges the solution space.

A. Active Polyhedrons Generation

Prior to the SFC construction, we leverage existing path searching algorithms JPS [20] to obtain a reference path that sequentially traverses through all waypoints $\mathbf{p}_{b,\lambda}^{\text{sp}}$ from the start to the end. Traditional construction methods [21] generate a sequence of continuously intersecting polyhedrons by identifying and linking the farthest unblocked points along the reference path. However, due to obstacle occlusion and environmental factors, this approach introduces significant uncertainties in polyhedron generation, leading to reduced feasible solution spaces, such as hollow areas between the surface and polyhedrons, as illustrated in Figure 4 (a). To address the challenge, we develop an active polyhedrons generation strategy that extends the polyhedron around constrained waypoints of interest, inspired by the method proposed in [35].

As illustrated in Figure 4 (a), we define an arbitrary and winding purple path that orderly connects the start point $\mathbf{p}_{b,o}$, several constrained waypoints $\mathbf{p}_{b,\lambda}^{\text{sp}}$, and the end point $\mathbf{p}_{b,f}$. For clarity, we focus on the situation at a single constrained point. According to the RILS method [36], the convex polyhedron is strongly related to the input straight line. This relationship naturally leads us to consider a key geometric constraint: constructing two straight lines that not only connect the constrained point to its previous and subsequent points, but crucially, both remain parallel to the plane. To determine the directions towards and away from the constrained points, we calculate the average of a given number of points before

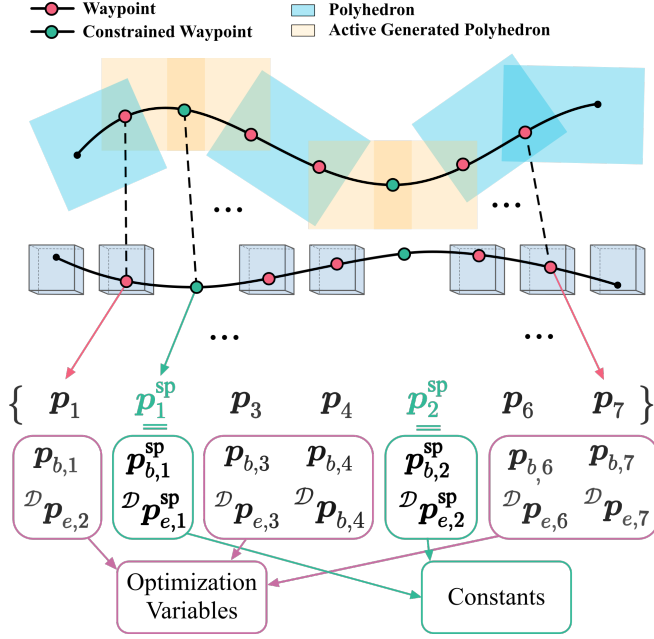


Fig. 5. Waypoint constraints implementation: our method sets constrained waypoints as constants while treating remaining waypoints as optimization variables, which differs from traditional temporal-spatial decomposition methods that optimize all waypoints simultaneously.

and after the constrained point along the path, denoted as $\mathbf{p}_1^{\text{avg}}$ and $\mathbf{p}_2^{\text{avg}}$ respectively, as shown in Figure 4 (b). These points are then projected onto an auxiliary plane parallel to the previous plane but passing through the constrained waypoint, resulting in two projected vectors $\mathbf{p}_1^{\text{proj}}$ and $\mathbf{p}_2^{\text{proj}}$ as illustrated in Figure 4 (c). After normalizing and scaling these vectors by r_p , we obtain two new generation points, $\mathbf{p}_1^{\text{ext}}$ and $\mathbf{p}_2^{\text{ext}}$. By connecting the constrained point to these generation points, two polyhedrons are actively generated and tightly attached to the plane, as illustrated in Figure 4 (d). Additionally, we define two jump points, $\mathbf{p}_1^{\text{jump}}$ and $\mathbf{p}_2^{\text{jump}}$, which are the first and last points along the path within these two polyhedrons respectively. Their specific applications will be discussed in the following subsection.

B. SFC Generation

After generating the polyhedrons described above, the initial SFC is constructed using the general method proposed by [36] along the path. When the iterative point reaches $\mathbf{p}_1^{\text{jump}}$, the iteration is immediately terminated, and two polyhedrons are added to the queue. The iteration then resumes from the corresponding $\mathbf{p}_2^{\text{jump}}$ and continues the generation process. Ultimately, we obtain the SFC in \mathcal{H} -representation as a series of consecutively intersected polyhedrons [21]:

$$\mathcal{S} := \bigcup_{i=1}^M \mathcal{H}_i \subset \mathbb{R}^3 \quad (16a)$$

$$\mathcal{H}_i := \{ \mathbf{x} \in \mathbb{R}^3 \mid \mathbf{A}_i \mathbf{x} \preceq \mathbf{b}_i \}. \quad (16b)$$

where M is the total number of polyhedrons.

IV. OPTIMIZATION FRAMEWORK

This section presents our optimization problem formulation and solution methodology. We begin by introducing our approach to handling waypoint constraints in \mathbb{R}^6 for both the aerial manipulator and end effector. Subsequently, we formulate the comprehensive objective function that balances control effort and time consumption metrics. The objective function is subject to multiple constraint categories: safety constraints implemented through dynamic approximation, attitude constraints derived by extending waypoint constraints from \mathbb{R}^6 to $\text{SE}(3) \times \mathbb{R}^3$, and fundamental dynamics and kinematic constraints. Finally, we detail the gradient propagation approach used to solve this optimization problem.

A. Waypoint Constraints Implementation

In this framework, we focus on generating a 6-dimensional trajectory $\mathbf{p}(t) = [\mathbf{p}_b^\top(t), \mathcal{D}\mathbf{p}_e^\top(t)]^\top \in \mathbb{R}^6$, where $\mathbf{p}_b(t)$ represents the aerial manipulator's trajectory in \mathcal{F}_W and $\mathcal{D}\mathbf{p}_e(t)$ describes the end-effector trajectory in \mathcal{F}_D . To implement waypoint constraints effectively, we first address the case of \mathbb{R}^6 waypoint constraints before extending to $\text{SE}(3) \times \mathbb{R}^3$.

For handling these constraints in spatio-temporal trajectories, we establish a systematic mapping approach that classifies spatial points as either constants or optimization variables, as shown in Figure 5. Following Equation (16a), we construct M polyhedrons that generate $M - 1$ intermediate points at their intersections. These intermediate points form the set $P_{\text{in}} := \{\mathbf{p}_1, \mathbf{p}_2, \dots, \mathbf{p}_{M-1}\}$, where each point $\mathbf{p}_i = [\mathbf{p}_{b,i}^\top, \mathcal{D}\mathbf{p}_{e,i}^\top]^\top \in \mathbb{R}^6$, for $i \in \{1, 2, \dots, M - 1\}$.

Within this framework, we predefine specific waypoints $\mathbf{p}_\lambda^{\text{sp}} \in \mathbb{R}^6$ for $\lambda \in \{1, 2, \dots, n_\Lambda\}$. Here, $\mathbf{p}_{b,\lambda}^{\text{sp}}$ is guaranteed to lie within polyhedron intersections through the method described in Section III-A, while $\mathcal{D}\mathbf{p}_{e,\lambda}^{\text{sp}}$ is confined to the workspace. The waypoint constraints are implemented by replacing the corresponding elements in P_{in} with these predefined points, which are then treated as constants.

To systematically identify optimization points, we define $\bar{M} = M - 1 - n_\Lambda$ as the number of points requiring optimization and establish a mapping through an index set $\Gamma := \{\gamma_1, \gamma_2, \dots, \gamma_{\bar{M}}\}$. Here, $\gamma_i \in \mathbb{N}^+$ denotes the index of the i -th optimization point in P_{in} , with $0 < \gamma_i < M$ for all $i \in \{1, 2, \dots, \bar{M}\}$. The points requiring optimization are thus represented as:

$$\mathcal{O} := \left\{ \mathbf{p}_i = \begin{bmatrix} \mathbf{p}_{b,i} \\ \mathcal{D}\mathbf{p}_{e,i} \end{bmatrix} \mid i \in \Gamma \right\}. \quad (17)$$

For computational efficiency, we separate all points in P_{in} , including the start point \mathbf{p}_o and end point \mathbf{p}_f , into two distinct components. We define matrices for both the aerial manipulator and the end effector:

$$\mathbf{P} = [\mathbf{p}_{b,0}, \mathbf{p}_{b,1}, \dots, \mathbf{p}_{b,M}]^\top \in \mathbb{R}^{(M+1) \times 3}, \quad (18a)$$

$$\mathbf{Q} = [\mathcal{D}\mathbf{p}_{e,0}, \mathcal{D}\mathbf{p}_{e,1}, \dots, \mathcal{D}\mathbf{p}_{e,M}]^\top \in \mathbb{R}^{(M+1) \times 3}. \quad (18b)$$

Using only the optimization points, we construct two additional matrices:

$$\bar{\mathbf{P}} = [\mathbf{p}_{b,\gamma_1}, \mathbf{p}_{b,\gamma_2}, \dots, \mathbf{p}_{b,\gamma_M}]^\top \in \mathbb{R}^{\bar{M} \times 3}, \quad (19a)$$

$$\bar{\mathbf{Q}} = [{}^D\mathbf{p}_{e,\gamma_1}, {}^D\mathbf{p}_{e,\gamma_2}, \dots, {}^D\mathbf{p}_{e,\gamma_M}]^\top \in \mathbb{R}^{\bar{M} \times 3}. \quad (19b)$$

Additionally, we define the temporal sequence vector as $\mathbf{T} = [T_1, T_2, \dots, T_M]^\top$. Following Equation (14), we introduce $\mathbf{C} = C(\Xi, \mathbf{T}) \in \mathbb{R}^{2Ms \times 6}$ as the polynomial parameter matrix, where $\Xi = [\mathbf{P}, \mathbf{Q}] \in \mathbb{R}^{(M-1) \times 6}$. For computational convenience, we split parameter matrix \mathbf{C} into $\mathbf{D} = [\mathbf{c}_{b,1}^\top, \dots, \mathbf{c}_{b,M}^\top]^\top \in \mathbb{R}^{2Ms \times 3}$ for the aerial manipulator and $\mathbf{E} = [\mathbf{c}_{e,1}^\top, \dots, \mathbf{c}_{e,M}^\top]^\top \in \mathbb{R}^{2Ms \times 3}$ for the end effector. To efficiently compute the gradients of the objective function with respect to \mathbf{P} , \mathbf{Q} , and \mathbf{T} , we first calculate the partial derivatives with respect to \mathbf{D} , \mathbf{E} , and \mathbf{T} , and then employ the chain rule for gradient propagation. Detailed derivations will be presented in Section IV-G.

B. Problem Formulation

Based on the waypoint constraints established above, we formulate the optimization problem as:

$$\min_{\mathbf{P}, \mathbf{Q}, \mathbf{T}} \mathcal{J} = \int_0^{T_\sigma} \|\mathbf{p}^{(s)}(t)\|^2 dt + \rho T_\sigma \quad (20a)$$

$$\text{s.t. } \mathcal{G}(\mathbf{p}(t), \dots, \mathbf{p}^{(s)}(t)) \preceq \mathbf{0}, \quad \forall t \in [0, T_\sigma] \quad (20b)$$

$$\mathbf{p}_1^{[s-1]}(0) = \mathbf{p}_o, \quad \mathbf{p}_M^{[s-1]}(T_M) = \mathbf{p}_f \quad (20c)$$

$$T_i > 0, \quad i \in \{1, 2, \dots, M\} \quad (20d)$$

where $T_\sigma = \sum_{i=1}^M T_i$ is the total time consumption with regularization factor $\rho > 0$, and \mathcal{G} denotes the inequality constraints over $[0, T_\sigma]$. The notation $\mathbf{p}^{[s-1]}$ represents the multi-order differentials matrix $[\mathbf{p}, \dot{\mathbf{p}}, \dots, \mathbf{p}^{(s-1)}] \in \mathbb{R}^{6 \times s}$. Let $\mathbf{p}_o, \mathbf{p}_f \in \mathbb{R}^{6 \times s}$ denote the initial and terminal conditions for the aerial manipulator in \mathcal{F}_W and the end effector in \mathcal{F}_D . T_i denotes the duration of the i -th segment, and M is the total number of segments.

The inequality constraints in Equation (20b) encompass multiple aspects, including safety, dynamic, kinematic and attitude constraints. We adopt a penalty-based approach to handle these constraints efficiently by incorporating them into the objective function with appropriate weights, thereby transforming the original constrained optimization problem into an unconstrained one. To reduce the computational complexity, we approximate the continuous integral using discrete numerical integration:

$$\int_0^{T_\sigma} J_G dt \approx \sum_{i=1}^M \sum_{n=0}^{N-1} \frac{T_i}{N} J_G^i\left(\frac{nT_i}{N}\right) \quad (21)$$

where J_G^i represents the soft penalty terms for the i -th segment, and N denotes the number of discretization points per segment.

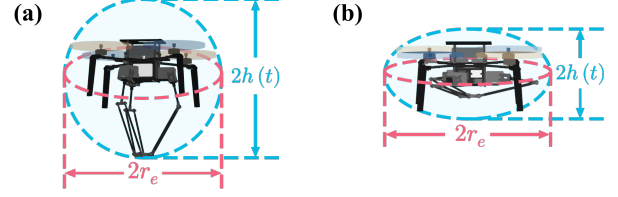


Fig. 6. Dynamic ellipsoid approximation results for different shapes, where the horizontal semi-major axis length r_e remains constant, while the vertical axis length $h(t)$ varies dynamically.

C. Control Effort and Total Time Penalty

We define the control effort penalty J_c as the integral of the squared third-order derivatives (i.e., minimum jerk) for both the aerial manipulator and the end effector. The total control effort is given by:

$$J_c = \int_0^{T_i} \|\mathbf{p}^{(3)}(t)\|^2 dt = \sum_{i=1}^M \int_0^{T_i} \|\mathbf{p}_i^{(3)}(t)\|^2 dt. \quad (22)$$

The partial derivatives of the i -th trajectory segment with respect to $\mathbf{c}_{x,i}$ and T_i can be derived as follows (where $x \in \{b, e\}$):

$$\frac{\partial J_c^i}{\partial \mathbf{c}_{x,i}} = 2 \int_0^{T_i} \boldsymbol{\beta}^{(3)}(t) \boldsymbol{\beta}^{(3)}(t)^\top \mathbf{c}_{x,i} dt, \quad (23)$$

$$\frac{\partial J_c^i}{\partial T_i} = \sum_x \left(\mathbf{c}_{x,i}^\top \boldsymbol{\beta}^{(3)}(T_i) \right)^\top \mathbf{c}_{x,i}^\top \boldsymbol{\beta}^{(3)}(T_i). \quad (24)$$

In addition, to ensure trajectory efficiency, we incorporate a time penalty term J_t , defined as the total trajectory duration:

$$J_t = T_\sigma = \sum_{i=1}^M T_i, \quad (25)$$

where T_i represents the duration of the i -th trajectory segment. The gradients of J_t^i with respect to the optimization variables are straightforward:

$$\frac{\partial J_t^i}{\partial \mathbf{c}_{b,i}} = \mathbf{0}_{6 \times 3}, \quad \frac{\partial J_t^i}{\partial \mathbf{c}_{e,i}} = \mathbf{0}_{6 \times 3}, \quad \frac{\partial J_t^i}{\partial T_i} = 1. \quad (26)$$

D. Safety Penalty

We extend the approaches proposed by [21] and [36] by modeling the entire aerial manipulator system as a dynamic ellipsoid during task execution. The ellipsoid, designed with fixed semi-major axes of length r_e in the xy -plane, incorporates a variational function $h(t)$ to dynamically adjust its length along the z -axis, accounting for the manipulator's motion range and ensuring complete coverage of the entire system, as shown in Figure 6. The formulation of this ellipsoidal model is given by:

$$\mathcal{E}(\boldsymbol{\xi}, t) = \mathbf{G}(t) \cdot (\mathbf{R}_B(t)\boldsymbol{\xi}) + \mathbf{p}_b(t), \quad \boldsymbol{\xi}^\top \boldsymbol{\xi} \leq 1, \quad (27a)$$

$$\mathbf{G}(t) = \text{diag}(r_e, r_e, h(t)) \in \mathbb{R}_{>0}^{3 \times 3}, \quad (27b)$$

$$h(t) = ({}^D\mathbf{p}_B - {}^D\mathbf{p}_e(t))^\top \mathbf{e}_3, \quad (27c)$$

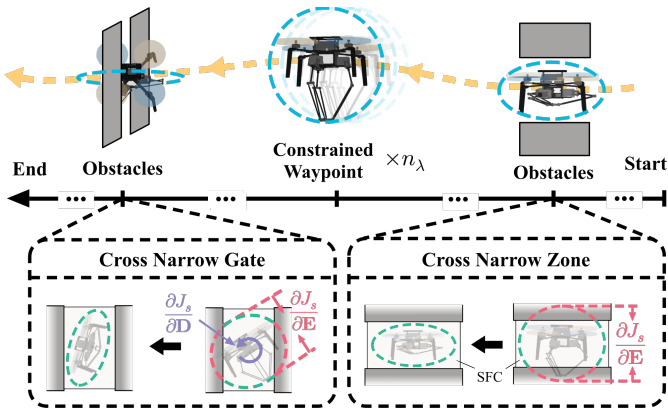


Fig. 7. Visualization of the safety penalty mechanism: The aerial manipulator achieves whole-body collision avoidance by optimizing its configuration through orientation adjustment and delta arm extension, while maintaining task constraints at specified waypoints within the SFC limits.

where $\xi \in \mathbb{R}^3$ represents any vector within a unit sphere, and \mathcal{E} represents the approximated ellipsoid in the world frame \mathcal{F}_W . The matrix $\mathbf{G}(t)$ encodes the semi-lengths of the ellipsoid's three axes along its diagonal. $e_3 = [0, 0, 1]^\top$ is the unit vector. ${}^D\mathbf{p}_B$ denotes the translation from \mathcal{F}_D to \mathcal{F}_B .

To guarantee safety, we constrain the dynamic ellipsoid to remain within the SFC using the aforementioned methodologies, as shown in Figure 7. This containment constraint can be mathematically expressed as:

$$\mathcal{E} \subset \mathcal{S} \quad (28)$$

where \mathcal{S} is the space defined in Equation (16a). To achieve this, we define the following penalty functions:

$$J_s = \sum_{i=1}^M \sum_{n=0}^{N-1} \sum_{k=1}^{K_i} \frac{T_i}{N} \mathcal{K}(\mathcal{P}_{s,i,n,k}), \quad (29a)$$

$$\mathcal{P}_{s,i,n,k} = \left(\mathbf{p}_{i,n}^k(\tau) - \hat{\mathbf{p}}_i^k \right)^\top \hat{\mathbf{n}}_i^k + d_s \quad (29b)$$

where $\tau = \frac{nT_i}{N}$, a definition that holds for all subsequent derivations. Here, $\mathcal{K}(\cdot)$ denotes the cubic smooth function defined as $\mathcal{K}(x) = \max(x^3, 0)$. For the i -th polyhedron containing K_i half-planes, $\hat{\mathbf{p}}_i^k$ represents an arbitrary point on the k -th half-plane with $\hat{\mathbf{n}}_i^k$ as its outward-pointing normal vector, and d_s defines a small safety margin. The term $\mathbf{p}_{i,n}^k$ represents the point on the ellipsoid's surface where its normal vector is perpendicular to the k -th plane. This point can be solved by inverting the ellipsoidal tangent point equation and be computed as follows:

$$\begin{cases} \mathbf{p}_{i,n}^k(\tau) = \mathbf{R}_{B,i}(\tau) \cdot {}^B\mathbf{p}_{i,n}^k(\tau) + \mathbf{p}_{b,i}(\tau), \\ {}^B\mathbf{p}_{i,n}^k(\tau) = \pm \frac{\mathbf{G}^2(\tau) \cdot (\mathbf{R}_{B,i}^\top(\tau) \hat{\mathbf{n}}_i^k)}{\left\| \mathbf{G}(\tau) \cdot (\mathbf{R}_{B,i}^\top(\tau) \hat{\mathbf{n}}_i^k) \right\|_2}, \\ {}^B\mathbf{p}_{i,n}^k(\tau) \cdot (\mathbf{R}_{B,i}^\top(\tau) \cdot \hat{\mathbf{n}}_i^k) \geq 0. \end{cases} \quad (30)$$

To simplify both expression and computation, we rewrite $\mathcal{P}_{s,i,n,k}(t)$ as:

$$\mathcal{P}_{s,i,n,k} = \mathcal{P}_s^\alpha + \mathcal{P}_s^\beta + d_s, \quad (31a)$$

$$\mathcal{P}_s^\alpha = \left(\mathbf{p}_{b,i}(\tau) - \hat{\mathbf{p}}_i^k \right)^\top \hat{\mathbf{n}}_i^k, \quad (31b)$$

$$\mathcal{P}_s^\beta = \left\| \mathbf{G}(\tau) \cdot (\mathbf{R}_B^\top(\tau) \hat{\mathbf{n}}_i^k) \right\|. \quad (31c)$$

where the term \mathcal{P}_s^α is directly related to $\mathbf{p}_{b,i}(\tau)$, while the term \mathcal{P}_s^β is closely coupled with both $\ddot{\mathbf{p}}_{b,i}(\tau)$ and ${}^D\mathbf{p}_{e,i}(\tau)$. Following these coupling relationships, we derive the gradient of the safety cost with respect to the optimization variables \mathbf{D} , \mathbf{E} , and \mathbf{T} :

$$\frac{\partial J_s}{\partial \mathbf{D}} = \frac{\partial \mathcal{P}_s^\alpha}{\partial \mathbf{p}_b} \frac{\partial \mathbf{p}_b}{\partial \mathbf{D}} + \frac{\partial \mathcal{P}_s^\beta}{\partial \ddot{\mathbf{p}}_b} \frac{\partial \ddot{\mathbf{p}}_b}{\partial \mathbf{D}} \quad (32)$$

$$\frac{\partial J_s}{\partial \mathbf{E}} = \frac{\partial \mathcal{P}_s^\beta}{\partial {}^D\mathbf{p}_e} \frac{\partial {}^D\mathbf{p}_e}{\partial \mathbf{E}} \quad (33)$$

$$\frac{\partial J_s}{\partial \mathbf{T}} = \frac{\partial \mathcal{P}_s^\alpha}{\partial \mathbf{p}_b} \frac{\partial \mathbf{p}_b}{\partial \mathbf{T}} + \frac{\partial \mathcal{P}_s^\beta}{\partial \ddot{\mathbf{p}}_b} \frac{\partial \ddot{\mathbf{p}}_b}{\partial \mathbf{T}} + \frac{\partial \mathcal{P}_s^\beta}{\partial {}^D\mathbf{p}_e} \frac{\partial {}^D\mathbf{p}_e}{\partial \mathbf{T}}. \quad (34)$$

E. Kinematics and Dynamics Penalty

To ensure the physical feasibility of the generated trajectories, we need to consider both kinematic and dynamic constraints. The kinematic constraints govern the system's workspace, velocities, and body rates, while the dynamic constraints regulate the thrust forces.

We first consider the kinematic constraints. For the delta arm to operate safely and effectively, its end effector must remain within a prescribed workspace. Following [8], we model this workspace as a cuboid in the Cartesian coordinate system, where $\kappa \in \{x, y, z\}$ denotes any of the three axes. The workspace is bounded by:

$$\kappa_{e,\ell} \leq \mathbf{e}_\kappa^\top {}^D\mathbf{p}_e(\tau) \leq \kappa_{e,u}, \quad (35a)$$

where $\kappa_{e,\ell}$ and $\kappa_{e,u}$ denote the lower and upper bounds along axis κ , respectively, and \mathbf{e}_κ represents the unit vector along the κ -axis. To enforce these workspace constraints, we introduce the following penalty terms:

$$J_k = \sum_{i=1}^M \sum_{n=0}^{N-1} \sum_{\kappa} \frac{T_i}{N} \left(\mathcal{K}(\mathcal{P}_{k_\ell,i,n,\kappa}) + \mathcal{K}(\mathcal{P}_{k_u,i,n,\kappa}) \right), \quad (36a)$$

$$\mathcal{P}_{k_\ell,i,n,\kappa} = \left(\mathbf{e}_\kappa^\top {}^D\mathbf{p}_{e,i}(\tau) \right)^2 - \kappa_{e,\ell}^2, \quad (36b)$$

$$\mathcal{P}_{k_u,i,n,\kappa} = \kappa_{e,u}^2 - \left(\mathbf{e}_\kappa^\top {}^D\mathbf{p}_{e,i}(\tau) \right)^2. \quad (36c)$$

To prevent excessive motion, we also constrain the velocities of both the aerial manipulator and the end effector. The aerial manipulator's velocity is limited to an upper bound $v_{b,u}$, while the end-effector velocity is constrained by $v_{e,u}$. These constraints are incorporated through the following penalty terms:

$$J_{k,vel} = \sum_{i=1}^M \sum_{n=0}^{N-1} \frac{T_i}{N} \left(\mathcal{K}(\mathcal{P}_{b,v,i,n}) + \mathcal{K}(\mathcal{P}_{e,v,i,n}) \right), \quad (37a)$$

$$\mathcal{P}_{b,v,i,n} = \left\| \dot{\mathbf{p}}_{b,i}(\tau) \right\|^2 - v_{b,u}^2, \quad (37b)$$

$$\mathcal{P}_{e,v,i,n} = \left\| {}^D\dot{\mathbf{p}}_{e,i}(\tau) \right\|^2 - v_{e,u}^2, \quad (37c)$$

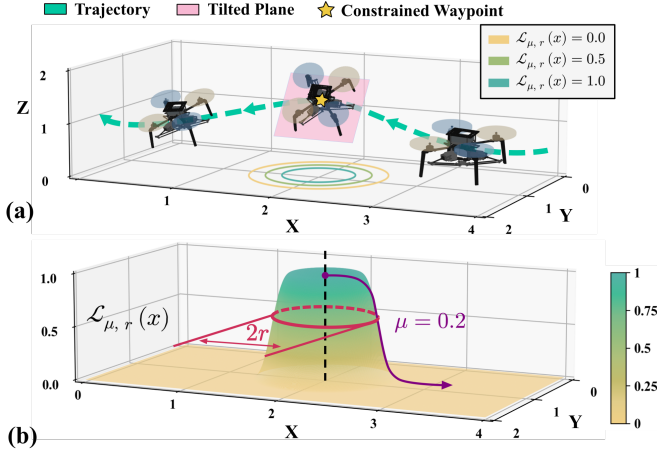


Fig. 8. Visualization of the relaxation function: (a) illustrates the aerial manipulator's smooth attitude adjustment; (b) depicts the relaxation function's continuous transition from 0 (no effect) to 1 (full activation) as the distance decreases, ensuring smooth gradients.

where $\dot{\mathbf{p}}_{b,i}(\tau)$ represents the velocity of the aerial manipulator in $\mathcal{F}_{\mathcal{W}}$, and ${}^{\mathcal{D}}\dot{\mathbf{p}}_{e,i}(\tau)$ represents the velocity of the end effector in $\mathcal{F}_{\mathcal{D}}$.

As another kinematic constraint, we consider the aerial manipulator's body rates. Given that yaw angle variations are neglected in our framework, we focus only on the body rates in the xy -plane. The corresponding penalty terms are defined as:

$$J_{k,bdr} = \sum_{i=1}^M \sum_{n=0}^{N-1} \frac{T_i}{N} \mathcal{K}(\mathcal{P}_{\omega,i,n}), \quad (38a)$$

$$\mathcal{P}_{\omega,i,n} = \|\mathcal{B}\omega_{xy,i}\|^2 - \omega_{xy,u}^2, \quad (38b)$$

where $\mathcal{B}\omega_{xy,i} = [\omega_x, \omega_y]^\top$ represents the body angular rates in the xy -plane, and $\omega_{xy,u}$ denotes the upper limit of the body rates.

For dynamic constraints, we consider the aerial manipulator's thrust capabilities. The normalized thrust f must remain within physically realizable bounds:

$$f_\ell \leq f \leq f_u, \quad (39)$$

where f_ℓ and f_u denote the lower and upper thrust limits. We formulate the corresponding penalty terms as:

$$J_{d,thr} = \sum_{i=1}^M \sum_{n=0}^{N-1} \frac{T_i}{N} \left(\mathcal{K}(\mathcal{P}_{f_u,i,n}) + \mathcal{K}(\mathcal{P}_{f_\ell,i,n}) \right), \quad (40a)$$

$$\mathcal{P}_{f_u,i,n} = \|\ddot{\mathbf{p}}_{b,i}(\tau) + g\mathbf{e}_3\|^2 - f_u^2, \quad (40b)$$

$$\mathcal{P}_{f_\ell,i,n} = f_\ell^2 - \|\ddot{\mathbf{p}}_{b,i}(\tau) + g\mathbf{e}_3\|^2, \quad (40c)$$

where $\ddot{\mathbf{p}}_{b,i}(\tau)$ denotes the aerial manipulator's acceleration.

The gradients of all kinematics and dynamics penalty terms with respect to the optimization variables \mathbf{D} , \mathbf{E} and \mathbf{T} can be efficiently computed using the method described in [37], [38].

F. Attitude Penalty

Attitude constraints are imposed at specified waypoints to extend the waypoint constraints from \mathbb{R}^6 to $\text{SE}(3) \times \mathbb{R}^3$. To

handle these constraints in a differentiable manner, we adopt a relaxation approach based on the work of [30]. This approach smoothly incorporates integer variables into our nonlinear programming model through a relaxation function defined as:

$$\mathcal{L}_{\mu,r}(x) = \begin{cases} 0, & x \leq -r\mu \\ \frac{1}{2\mu^4} \left(\frac{x-r}{r} + \mu \right)^3 \left(\mu - \frac{x-r}{r} \right), & -r\mu < x \leq 0 \\ \frac{1}{2\mu^4} \left(\frac{x-r}{r} - \mu \right)^3 \left(\mu + \frac{x-r}{r} \right) + 1, & 0 < x \leq r\mu \\ 1, & x > r\mu \end{cases} \quad (41)$$

where μ controls the smoothness of the function and r determines the scope radius. The behavior of this smooth function is illustrated in Figure 8.

For waypoints with specified positions $\mathbf{p}_{b,\lambda}^{\text{sp}}$ and orientations $\mathbf{n}_\lambda^{\text{sp}}$, we incorporate these constraints into the penalty term:

$$J_a = \sum_{i=1}^M \sum_{n=0}^{N-1} \sum_{\lambda=1}^{n_\lambda} \frac{T_i}{N} \mathcal{L}_{\mu,r}(d_{i,n,\lambda}) \mathcal{K}(\mathcal{P}_{a,i,n,\lambda}), \quad (42a)$$

$$d_{i,n,\lambda} = \|\mathbf{p}_{b,i}(\tau) - \mathbf{p}_{b,\lambda}^{\text{sp}}\|^2, \quad (42b)$$

$$\mathcal{P}_{a,i,n,\lambda} = \|\mathbf{f}_i(\tau) - \|\mathbf{f}_i(\tau)\| \mathbf{n}_\lambda^{\text{sp}}\|^2 - \bar{e}^2, \quad (42c)$$

$$\mathbf{f}_i(\tau) = \ddot{\mathbf{p}}_{b,i}(\tau) + g\mathbf{e}_3, \quad (42d)$$

where $d_{i,n,\lambda}$ represents the Euclidean distance to each specific point, \bar{e} denotes the maximum allowable angle difference and $\mathbf{f}_i(\tau)$ represents the thrust vector at time τ . The gradient of the penalty term J_a with respect to the optimization variables can then be computed as:

$$\frac{\partial J_a}{\partial \mathbf{D}} = \frac{\partial J_a}{\partial \mathbf{p}_b} \frac{\partial \mathbf{p}_b}{\partial \mathbf{D}} + \frac{\partial J_a}{\partial \ddot{\mathbf{p}}_b} \frac{\partial \ddot{\mathbf{p}}_b}{\partial \mathbf{D}}, \quad (43)$$

$$\frac{\partial J_a}{\partial \mathbf{T}} = \frac{\partial J_a}{\partial \mathbf{p}_b} \frac{\partial \mathbf{p}_b}{\partial \mathbf{T}} + \frac{\partial J_a}{\partial \ddot{\mathbf{p}}_b} \frac{\partial \ddot{\mathbf{p}}_b}{\partial \mathbf{T}}. \quad (44)$$

G. Gradient Propagation

Based on the preceding formulation, we establish the complete objective function \mathcal{J} that incorporates the control effort, regularized time, and soft constraint penalties. Having calculated the complete partial derivatives of \mathcal{J} with respect to the parameter matrices \mathbf{D} , \mathbf{E} , and \mathbf{T} , we now leverage their relationship with the parameter matrix $\mathbf{C} = \mathcal{C}(\mathbf{E}, \mathbf{T})$ to propagate the gradients to the intermediate points $\mathbf{\Xi} = [\mathbf{P}, \mathbf{Q}]$. Since $\mathbf{P} \subset \mathbf{P}$ and $\mathbf{Q} \subset \mathbf{Q}$ represent reduced intermediate points, we derive their respective gradients using the chain rule:

$$\frac{\partial \mathcal{J}(\mathbf{P}, \mathbf{Q}, \mathbf{T})}{\partial \mathbf{P}} = \frac{\partial \mathcal{J}}{\partial \mathbf{D}} \frac{\partial \mathbf{D}}{\partial \mathbf{\Xi}} \frac{\partial \mathbf{\Xi}}{\partial \mathbf{P}}, \quad (45)$$

$$\frac{\partial \mathcal{J}(\mathbf{P}, \mathbf{Q}, \mathbf{T})}{\partial \mathbf{Q}} = \frac{\partial \mathcal{J}}{\partial \mathbf{E}} \frac{\partial \mathbf{D}}{\partial \mathbf{\Xi}} \frac{\partial \mathbf{\Xi}}{\partial \mathbf{Q}}, \quad (46)$$

$$\frac{\partial \mathcal{J}(\mathbf{P}, \mathbf{Q}, \mathbf{T})}{\partial \mathbf{T}} = \frac{\partial \mathcal{J}}{\partial \mathbf{T}} + \frac{\partial \mathcal{J}}{\partial \mathbf{D}} \cdot \frac{\partial \mathbf{D}}{\partial \mathbf{T}} + \frac{\partial \mathcal{J}}{\partial \mathbf{E}} \cdot \frac{\partial \mathbf{E}}{\partial \mathbf{T}}. \quad (47)$$

For computational efficiency, we adapt and extend the method from [29]. The original approach is directly applicable for calculating the partial gradient with respect to \mathbf{T} . For

gradients with respect to $\bar{\mathbf{P}}$ and $\bar{\mathbf{Q}}$, we develop a modified computation:

$$\frac{\partial \mathcal{J}}{\partial \bar{\mathbf{X}}} = \left(\mathbf{G}_{\gamma_1}^\top e_1, \mathbf{G}_{\gamma_2}^\top e_1, \dots, \mathbf{G}_{\gamma_M}^\top e_1 \right), \quad (48)$$

where \mathbf{G} follows the same definition and computation process as in Equation (63) in [29], and $\bar{\mathbf{X}} \in \bar{\mathbf{P}}, \bar{\mathbf{Q}}$. Additionally, we implement the constraint elimination technique to handle both spatial constraints in Equations (45) and (46) and temporal constraints in Equation (47), thereby enhancing computational efficiency. The resulting optimization problem is then solved using L-BFGS.

V. EXPERIMENTS

We evaluate the performance of our whole-body integrated motion planning framework through comprehensive experiments conducted in both simulation and real-world environments. Our evaluation consists of three main components: 1) ablation studies on the dynamic approximation module across three obstacle-rich scenarios to demonstrate its effectiveness, 2) simulation tests with multiple waypoint constraints on various inclined surfaces to analyze the framework’s effectiveness, and 3) real-world validation through balloon puncturing tasks performed on different inclined surfaces.

Our system is implemented in C++11 on Ubuntu 20.04 with ROS Noetic. As illustrated in Figure 9, the experimental platform integrates an NVIDIA Jetson Orin NX 16GB as the onboard computer and an NxtPX4v2 flight controller on a quadrotor equipped with a delta arm. The delta arm utilizes three DYNAMIXEL XL430-W250-T servo motors and features a needle end effector for precise manipulation tasks. The system’s state estimation relies on an Extended Kalman Filter (EKF) to fuse data from the NOKOV Motion Capture System and an IMU. We employ a separated control framework similar to [31] that supports error compensation for the aerial manipulator through end-effector adjustments.

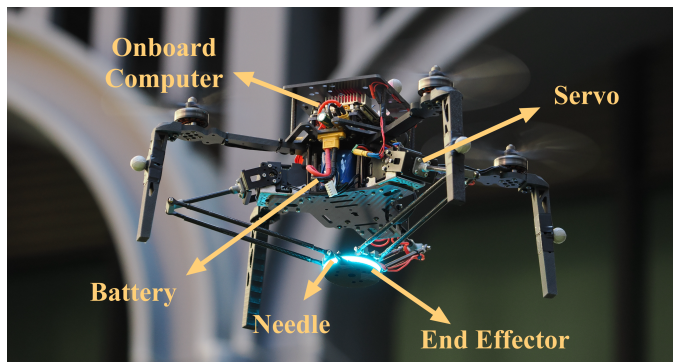


Fig. 9. Real-world aerial manipulator platform used for validation.

A. Ablation Study

To validate the effectiveness of our dynamic ellipsoidal approximation module within the whole-body integrated motion planning framework, we conduct a series of ablation studies. These studies evaluate the framework’s ability to generate collision-free trajectories under various initial configurations

TABLE I
DELTA ARM PARAMETERS

Notation	Value	Description
r_s	0.067 m	Static platform circumradius
r_d	0.024 m	End-effector circumradius
L_u	0.100 m	Upper arm length
L_l	0.160 m	Lower arm length

TABLE II
ABLATION STUDY ON CROSSING DIFFERENT GATE HEIGHTS

Method	Metric	Gate Height (m)							
		0.60	0.55	0.50	0.45	0.40	0.35	0.30	0.25
Prop.	Avail.	✓	✓	✓	✓	✓	✓	✓	✓
	Min. $2h(t)$ (m)	0.471	0.447	0.402	0.378	0.320	0.282	0.238	0.220
Abl.	Avail.	✓	✓	✓	✗	✗	✗	✗	✗
	Min. $2h(t)$ (m)	0.480	0.480	0.480	0.480	0.480	0.480	0.480	0.480

of the delta arm in obstacle-rich environments. For clarity, we define the method without the dynamic approximation module as **Ablated** and the method incorporating the dynamic approximation module as **Proposed**. Throughout these studies, we refer to the initial and final configurations of the delta arm as the **Bound** states. The x , y , and z components of vector ${}^{\mathcal{D}}\mathbf{p}_e$ are denoted as ${}^{\mathcal{D}}p_{ex}$, ${}^{\mathcal{D}}p_{ey}$, and ${}^{\mathcal{D}}p_{ez}$, respectively. The position along the z -axis of the end effector, ${}^{\mathcal{D}}p_{ez}$, directly influences the collision volume approximation element $h(t)$, as shown in Equation (27c). Given this relationship, our ablation studies focus primarily on modifying the bound states of the end effector along the z -axis and analyzing its variations throughout the process. Before presenting the experimental results, we establish the key parameters of our delta arm system as listed in Table I. The workspace along the z -axis in frame $\mathcal{F}_{\mathcal{D}}$ is constrained within $-0.22 \text{ m} \leq {}^{\mathcal{D}}p_{ez} \leq -0.07 \text{ m}$. The translation vector ${}^{\mathcal{D}}\mathbf{p}_{\mathcal{B}}$ from frame $\mathcal{F}_{\mathcal{D}}$ to frame $\mathcal{F}_{\mathcal{B}}$ is set to $[0, 0, 0.04]^\top$ m. Using these parameters, we conduct three distinct ablation experiments, as illustrated in Figure 10 and detailed in the following sections.

1) **Narrow Gate**: In the first ablation study, illustrated in Figure 10 (a) and (b), we set up a single narrow gate for each trial, with the gate height varying across different tests. Gate heights are uniformly sampled, ranging from 0.60 m to 0.25 m, as shown in the "Gate Height" row of Table II. The start and end positions for the aerial manipulator are placed on opposite sides of the gate to guide it through the gate. The chosen bound state of the end effector is deliberately set to ${}^{\mathcal{D}}p_{ez} = -0.20$ m. For the ablated method, the dynamic approximation module is removed, and the collision volume of the aerial manipulator is modeled using a constant ellipsoid. The major axis of this constant ellipsoid along the z -axis, $2h(t)$, is fixed at 0.48 m.

The results are summarized in Table II, where collision-free trajectories are marked with "✓" and collision trajectories with "✗". $\text{Min.}2h(t)$ denotes the minimum length of the major axis of the dynamic ellipsoid along the z -axis, as depicted in Figure 6. Our experimental results demonstrate that the aerial manipulator, equipped with our dynamic approximation module, successfully navigates through all narrow gates. Moreover, the $\text{Min.}2h(t)$ values decrease progressively with reduced gate heights, due to the optimal control effort input that enables

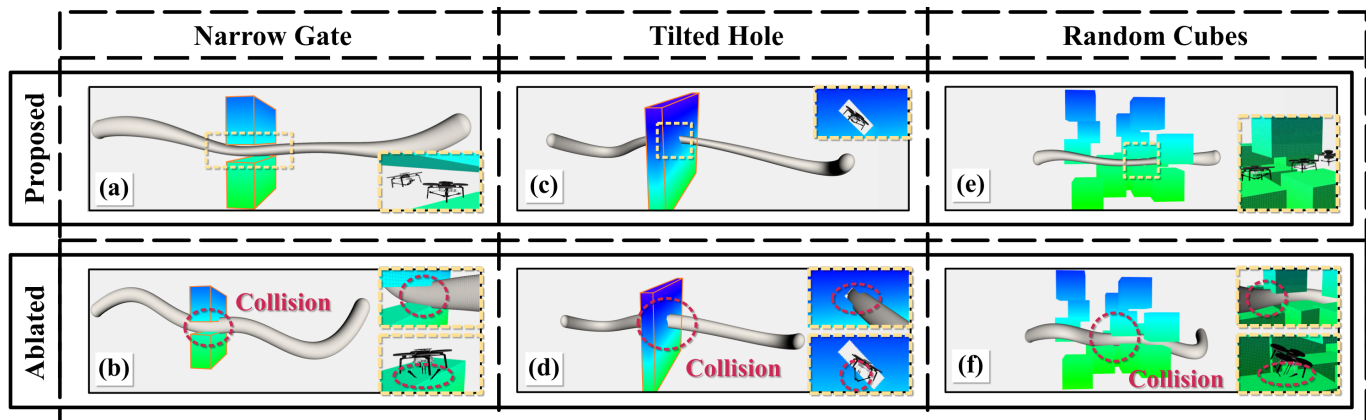


Fig. 10. Experimental validation of our trajectory planning framework with dynamic approximation. (a) shows the swept volume under dynamic approximation in the Narrow Gate scenario. (b) illustrates the ablation study, clearly showing that without our dynamic approximation module, the delta arm fails to retract and results in collision. (c) and (d) demonstrate the effectiveness of our method even under large attitude variations. (e) and (f) showcase that only our proposed method successfully navigates through narrow gaps in random cube environments without collisions.

TABLE III
ABLATION STUDY ON CROSSING DIFFERENT TILTED HOLES UNDER VARYING BOUND STATES

Method	Inclination ($^{\circ}$)	20			40			60			
		Bound $2h(t)$ (m)	0.22	0.34	0.48	0.22	0.34	0.48	0.22	0.34	0.48
Proposed	Avail.	✓	✓	✓	✓	✓	✓	✓	✓	✓	✓
	Min. $2h(t)$ (m)	0.22	0.22	0.23	0.22	0.22	0.22	0.22	0.22	0.22	0.22
	Max. Atti. ($^{\circ}$)	12.6	12.6	12.6	38.9	37.7	38.8	45.2	44.9	44.7	
Ablation	Avail.	✓	✗	✗	✓	✗	✗	✓	✗	✗	✗
	Min. $2h(t)$ (m)	0.22	0.34	0.48	0.22	0.34	0.48	0.22	0.34	0.48	
	Max. Atti. ($^{\circ}$)	11.8	-	-	37.1	-	-	42.8	-	-	

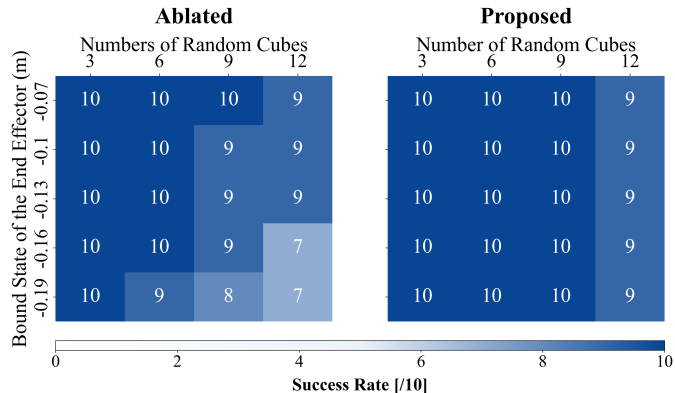


Fig. 11. Success rate comparison between the proposed and ablated methods. The proposed method consistently achieves higher success rates across all test conditions.

adaptive adjustments that eliminate the need to retract the delta arm totally for every gate crossing. In contrast, when tested with the ablated method, the end-effector position along the z -axis remains constant, resulting in a fixed $2h(t)$ of 0.48 m. This limitation prevents the aerial manipulator from passing through gates with heights less than or equal to 0.45 m.

2) **Tilted Hole:** The second ablation study, presented in Figure 10 (c) and (d), evaluates our method's performance in navigating through tilted rectangular holes with varying attitudes and bound arm states. The rectangular hole measures 0.80 m in length and 0.30 m in width, with inclination angles

of 20° , 40° , and 60° . For each inclination angle, we test three different bound end-effector positions (${}^{\mathcal{D}}p_{ez} = -0.07, -0.14, \text{ and } -0.20$ m), corresponding to bound ellipsoidal heights $2h(t)$ of 0.22 m, 0.34 m, and 0.48 m respectively.

The results are summarized in Table III, where we track two key metrics: the minimum ellipsoidal height (Min. $2h(t)$) and the maximum attitude angle relative to the horizon plane (Max.Atti.). Our proposed method with dynamic approximation successfully navigates through all hole configurations, regardless of inclination angles or bound states. Notably, when passing through the tilted hole, the aerial manipulator maintains a maximum attitude slightly different from being parallel to the hole's tilt while retracting the delta arm to its minimum, despite the available space within the hole allowing for more extended arm configurations. This behavior emerges from the optimization's trade-off between attitude adjustment and delta arm retraction energy costs. In contrast, the ablated method with fixed approximation volume succeeds only when the bound arm extension is minimal ($2h(t) = 0.22$ m). It fails in scenarios with larger bound states ($2h(t) = 0.34$ m and 0.48 m) across all inclination angles, as it lacks the capability to adaptively adjust the end-effector extension for navigating through rectangular holes.

3) **Random Cubes:** The third ablation study, illustrated in Figure 10 (e) and (f), evaluates our method's performance in complex environments with multiple obstacle cubes. The test environments are constructed with varying numbers of cubic obstacles (3, 6, 9, and 12 cubes), each with a side length of 0.80 m. For each obstacle configuration, we generate 10 random maps and evaluate the performance across different bound arm states (${}^{\mathcal{D}}p_{ez} = -0.07, -0.10, -0.13, -0.16$ and -0.19 m).

The results are visualized in the heatmap shown in Figure 11, where we compare the success rates between our proposed method and the ablated method. Our proposed method maintains consistently higher success rates across various environmental complexities and bound arm states. This superior performance is particularly evident in dense obstacle scenarios, where the ablated method experiences significant performance

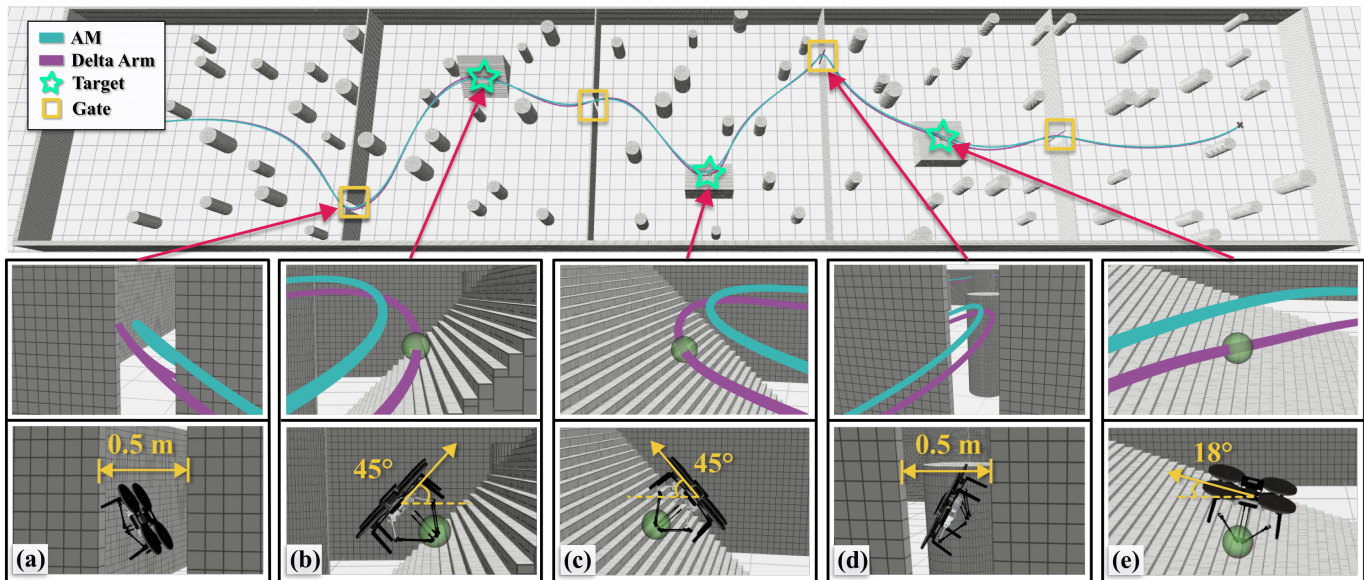


Fig. 12. Visualization of planned trajectories for an aerial manipulator system in a complex environment. The main figure shows the complete environment setup containing 3 constrained waypoints and 4 narrow gates, where the blue trajectory represent the quadrotor trajectory and the purple trajectory indicate the delta arm trajectory. Five local enlarged views are presented to demonstrate the system’s performance. Upper rows display trajectory execution plots, while lower rows present corresponding simulation snapshots. These enlarged views demonstrate key behaviors: (a) and (d) show the system’s automatic arm retraction capability when passing through narrow gates for collision avoidance; (b), (c), and (e) illustrate the aerial manipulator maintaining a parallel attitude along inclined surfaces while keeping the delta arm at desired states to reach targets.

degradation, especially with extended delta arm configurations (i.e., smaller ${}^D p_{ez}$ values). However, it is worth noting that in one instance of the 12-cube scenarios, our method encounters a failure case. This failure occurs when the front-end planner generates an initial path through an extremely narrow passage that is spatially infeasible. Although the trajectory converges to a local optimum during optimization, the fundamental spatial constraints of the initial path lead to an inevitable collision.

B. Complex Environment Simulation

To validate our whole-body planning framework with high-order waypoint constraints, we design a challenging environment addressing two key objectives: collision-free flight through complex environments and precise passage through specific points with desired attitudes and end-effector states. The testing environment consists of a 100-meter corridor containing dense obstacle columns, four narrow gates, and three inclined surfaces. Each inclined surface has a target sphere positioned above it, as illustrated in Figure 12. The surface inclination angles and target sphere positions are known beforehand.

The task requires the aerial manipulator to touch three targets with its end effector while maintaining an attitude parallel to the respective surfaces. Given the system’s redundancy with 9 DoFs, this study does not focus on determining the optimal configuration for the task. Instead, we manually specify the $SE(3) \times \mathbb{R}^3$ waypoint constraints. To mitigate ground effect disturbances near inclined surfaces, we aim to maximize the end-effector extension. However, the end effector can compensate for aerial manipulator errors, which requires sufficient redundancy in the xy -plane to achieve

higher precision. Balancing these requirements, we set the end-effector extension to ${}^D p_{ez} = -0.20$ m, which provides both adequate distance from the inclined surfaces and necessary positioning redundancy for error compensation.

Using this configuration, we employ inverse kinematics to determine the aerial manipulator’s positions while maintaining parallel attitudes to the inclined surfaces, generating three specific waypoints p_λ^{sp} and corresponding orientations n_λ^{sp} , where $\lambda \in \{1, 2, 3\}$.

As shown in Figure 12, the trajectory satisfies waypoint constraints while ensuring collision-free motion. At Figure 12 (a) and (d), the system crosses narrow gates with large attitude changes and retracted delta arms, reflecting a balance between control effort and safety penalties. Furthermore, at Figure 12 (b), (c), and (e), the attitudes achieve the desired parallel alignment with respective surfaces, demonstrating successful algorithm convergence.

C. Real-world Validation

To demonstrate our whole-body integrated planning framework in real-world scenarios, we conduct experiments using the aerial manipulation platform shown in Figure 9. In these experiments, we place balloons on inclined surfaces and guide the aerial manipulator to pierce them with its end effector while maintaining alignment with the surface. We test various surface inclination angles and sequential waypoint constraints across different obstacle environments.

In our setup, the aerial manipulator begins and ends with a fully retracted arm configuration (${}^D p_{ez} = -0.07$ m) to facilitate safer takeoff. Following the method described in Section V-B, we calculate the desired $SE(3) \times \mathbb{R}^3$ waypoint constraints and apply them to trajectory generation. Due to

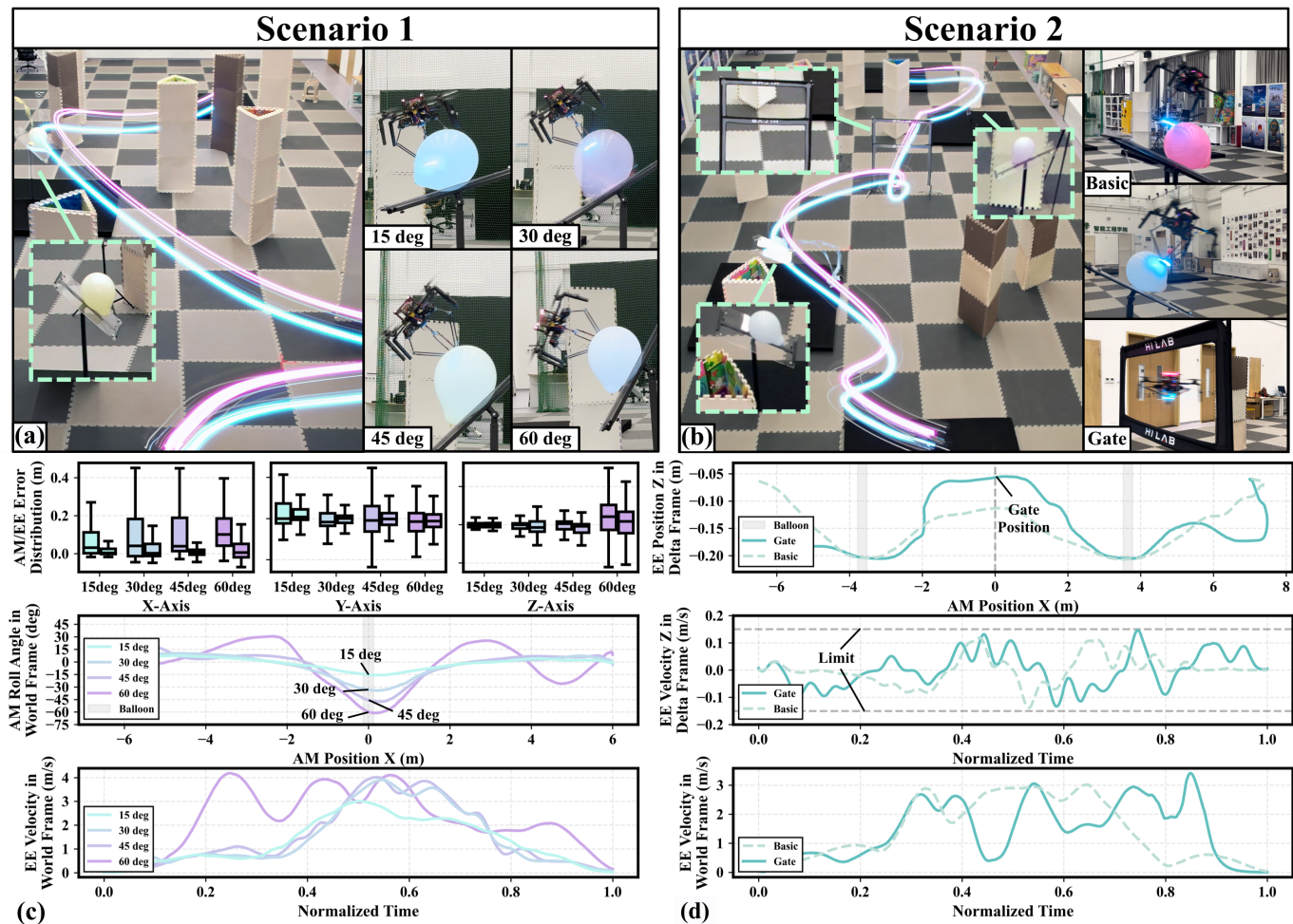


Fig. 13. Visualization of real-world experimental results for the aerial manipulator and the End Effector (EE). (a) shows the trajectories of the aerial manipulator in Scenario 1, where the purple line represents the base trajectory and the blue line indicates the end-effector trajectory. The four adjacent snapshots capture the aerial manipulator configurations immediately before balloon contact at 15 deg, 30 deg, 45 deg, and 60 deg. (b) presents the aerial manipulator trajectories in Scenario 2, which includes both Basic and Gate experiments. (c) illustrates the experimental results for Scenario 1: the first subplot shows tracking errors along three axes, where each group compares the aerial manipulator error (left) with the end-effector error (right); the second subplot displays the roll angle variation; and the third subplot shows the end-effector velocity in frame \mathcal{F}_W . (d) demonstrates the results for Scenario 2: the first and second subplots show the end-effector position and velocity along the z -axis in frame \mathcal{F}_D , respectively, while the third subplot presents the end-effector velocity in frame \mathcal{F}_W .

hardware limitations in sensing capabilities, we utilize a pre-built point cloud map to represent the environment, with the positions and orientations of inclined surfaces provided by the motion capture system.

1) *Different Inclined Angles*: As illustrated in Figure 13 (a), we position the inclined surface at a fixed location within a complex, obstacle-rich environment. The surface is oriented perpendicular to the yz -plane of the world frame \mathcal{F}_W to better observe attitude changes from roll angles across constrained waypoints. To comprehensively evaluate system capabilities, we test inclination angles of 15°, 30°, 45°, and 60°. We enable the compensation method to verify that the aerial manipulator can achieve higher precision with the delta arm in this balloon piercing task.

As demonstrated in the four images on the right side of Figure 13 (a), the aerial manipulator successfully achieves parallel alignment with the inclined surfaces and pierces the balloons with the needle. The tracking performance analysis, presented in the first subplot of Figure 13 (c), shows tracking errors

along the x , y , and z axes. The results demonstrate significant error compensation by the end effector, particularly during high-attitude manipulation scenarios, leading to enhanced precision. The second subplot illustrates the roll angle variations across all four experiments, with angles closely aligning with corresponding values in the balloon region. The third subplot, showing end-effector velocity in \mathcal{F}_W , demonstrates successful balloon piercing at velocities up to 4 m/s, indicating highly efficient performance, especially in an indoor environment.

2) *Sequential Waypoint Navigation*: As shown in Figure 13 (b), we design two experimental configurations: **Basic** and **Gate**. In Basic, the aerial manipulator sequentially pierces two balloons placed on inclined surfaces that are perpendicular to the yz -plane of \mathcal{F}_W . In Gate, we add a narrow racing gate between the balloons, requiring the system to retract its delta arm while passing through before piercing the second balloon. To evaluate the framework's inherent performance, we conduct these trials without end-effector compensation, particularly focusing on the trajectory along z_D .

Performance results are presented in Figure 13 (b), with key moments shown in the right portion. The first subplot of Figure 13 (d) illustrates the end-effector position along the z -axis in frame \mathcal{F}_D , demonstrating successful achievement of desired configurations in balloon regions. When crossing the gate, the Gate experiments show complete delta arm retraction, while Basic requires only minimal retraction, validating our framework's control effort optimality. The second subplot confirms that end-effector velocity remains within our 0.15 m/s constraint. The third subplot, showing end-effector velocity in \mathcal{F}_W , demonstrates successful collision-free motion and waypoint constraint fulfillment in a complex environment at velocities up to 3 m/s, validating our framework's effectiveness in real-world applications.

VI. CONCLUSION

This paper introduces a novel whole-body integrated motion planning framework for aerial manipulators that jointly optimizes the motions of the quadrotor and the manipulator. The framework considers different delta arm configurations and constructs a dynamic ellipsoid to approximate the entire collision volume, while incorporating multiple $SE(3) \times \mathbb{R}^3$ waypoint constraints to accommodate various manipulation tasks. Through extensive simulation experiments, we demonstrate that the proposed framework effectively converges in complex environments, ensuring collision avoidance across different delta arm configurations while meeting multiple waypoint constraints. The real-world experiments validate our framework's practical effectiveness, demonstrating high-speed manipulation capabilities and efficient trajectory generation in complex environments. Although our framework is specifically developed and validated on aerial manipulators with delta arms, the underlying dynamic ellipsoid approximation methodology can be generalized to various aerial systems with deformable structures. Building upon these results, future research will explore advanced manipulation tasks such as grasping and throwing, as well as improving control precision during aggressive maneuvers.

REFERENCES

- [1] A. Ollero, M. Tognon, A. Suarez, D. Lee, and A. Franchi, "Past, present, and future of aerial robotic manipulators," vol. 38, no. 1, pp. 626–645. [Online]. Available: <https://ieeexplore.ieee.org/document/9462539>
- [2] K. Zhang, P. Chermprayong, F. Xiao, D. Tzoumanikas, B. Dams, S. Kay, B. B. Kocer, A. Burns, L. Orr, T. Alhinai, C. Choi, D. D. Darekar, W. Li, S. Hirschmann, V. Soana, S. A. Ngah, C. Grillot, S. Sareh, A. Choubey, L. Margheri, V. M. Pawar, R. J. Ball, C. Williams, P. Shepherd, S. Leutenegger, R. Stuart-Smith, and M. Kovac, "Aerial additive manufacturing with multiple autonomous robots," vol. 609, no. 7928, pp. 709–717. [Online]. Available: <https://www.nature.com/articles/s41586-022-04988-4>
- [3] M. Trujillo, J. R. Martinez-de Dios, C. Martn, A. Viguria, and A. Ollero, "Novel aerial manipulator for accurate and robust industrial NDT contact inspection: A new tool for the oil and gas inspection industry," vol. 19, no. 6, p. 1305. [Online]. Available: <https://www.mdpi.com/1424-8220/19/6/1305>
- [4] W. Luo, J. Chen, H. Ebel, and P. Eberhard, "Time-optimal handover trajectory planning for aerial manipulators based on discrete mechanics and complementarity constraints," vol. 39, no. 6, pp. 4332–4349. [Online]. Available: <https://ieeexplore.ieee.org/document/10224341>
- [5] K. Hang, X. Lyu, H. Song, J. A. Stork, A. M. Dollar, D. Kragic, and F. Zhang, "Perching and resting paradigm for UAV maneuvering with modularized landing gears," vol. 4, no. 28, p. eaau6637. [Online]. Available: <https://www.science.org/doi/10.1126/scirobotics.aau6637>
- [6] M. Xu, Q. De, D. Yu, A. Hu, Z. Liu, and H. Wang, "Biomimetic morphing quadrotor inspired by eagle claw for dynamic grasping," *IEEE Transactions on Robotics*, vol. 40, pp. 2513–2528, 2024.
- [7] J. Thomas, J. Polin, K. Sreenath, and V. Kumar, "Avian-inspired grasping for quadrotor micro UAVs," in *Volume 6A: 37th Mechanisms and Robotics Conference*. American Society of Mechanical Engineers, p. V06AT07A014.
- [8] H. Cao, J. Shen, C. Liu, B. Zhu, and S. Zhao, "Motion planning for aerial pick-and-place with geometric feasibility constraints," pp. 1–18. [Online]. Available: <https://ieeexplore.ieee.org/document/10486851/>
- [9] H. Lee, H. Kim, and H. J. Kim, "Planning and control for collision-free cooperative aerial transportation," vol. 15, no. 1, pp. 189–201. [Online]. Available: <http://ieeexplore.ieee.org/document/7589023/>
- [10] M. Wang, Z. Chen, K. Guo, X. Yu, Y. Zhang, L. Guo, and W. Wang, "Millimeter-level pick and peg-in-hole task achieved by aerial manipulator," vol. 40, pp. 1242–1260. [Online]. Available: <https://ieeexplore.ieee.org/document/10339889/>
- [11] Y. Chen, J. Liang, Y. Wu, Z. Miao, H. Zhang, and Y. Wang, "Adaptive sliding-mode disturbance observer-based finite-time control for unmanned aerial manipulator with prescribed performance," vol. 53, no. 5, pp. 3263–3276. [Online]. Available: <https://ieeexplore.ieee.org/document/9768118/>
- [12] H. Cao, Y. Li, C. Liu, and S. Zhao, "ESO-based robust and high-precision tracking control for aerial manipulation."
- [13] M. Spahn, B. Brito, and J. Alonso-Mora, "Coupled mobile manipulation via trajectory optimization with free space decomposition," in *2021 IEEE International Conference on Robotics and Automation (ICRA)*. IEEE, pp. 12 759–12 765. [Online]. Available: <https://ieeexplore.ieee.org/document/9561821/>
- [14] E. Cuniato, I. Geles, W. Zhang, O. Andersson, M. Tognon, and R. Siegwart, "Learning to open doors with an aerial manipulator," in *2023 IEEE/RSJ International Conference on Intelligent Robots and Systems (IROS)*, 2023, pp. 6942–6948.
- [15] C. A. Dimmig and M. Kobilarov, "Non-prehensile aerial manipulation using model-based deep reinforcement learning," in *2024 IEEE 20th International Conference on Automation Science and Engineering (CASE)*, 2024, pp. 2194–2200.
- [16] R. Spica, A. Franchi, G. Oriolo, H. H. Bulthoff, and P. R. Giordano, "Aerial grasping of a moving target with a quadrotor UAV," in *2012 IEEE/RSJ International Conference on Intelligent Robots and Systems*. IEEE, pp. 4985–4992. [Online]. Available: <http://ieeexplore.ieee.org/document/6385771/>
- [17] D. Mellinger, Q. Lindsey, M. Shomin, and V. Kumar, "Design, modeling, estimation and control for aerial grasping and manipulation," in *2011 IEEE/RSJ International Conference on Intelligent Robots and Systems*. IEEE, pp. 2668–2673. [Online]. Available: <http://ieeexplore.ieee.org/document/6094871/>
- [18] M. Yavari, K. Gupta, and M. Mehrandezh, "Interleaved predictive control and planning for an unmanned aerial manipulator with on-the-fly rapid re-planning in unknown environments," vol. 20, no. 3, pp. 1690–1705. [Online]. Available: <https://ieeexplore.ieee.org/document/9844664/>
- [19] J.-P. Sleiman, F. Farshidian, and M. Hutter, "Versatile multicontact planning and control for legged loco-manipulation," *Science Robotics*, vol. 8, no. 81, p. eadg5014, 2023. [Online]. Available: <https://www.science.org/doi/abs/10.1126/scirobotics.adg5014>
- [20] S. Liu, K. Mohta, N. Atanasov, and V. Kumar, "Search-based motion planning for aggressive flight in SE(3)," vol. 3, no. 3, pp. 2439–2446. [Online]. Available: <http://ieeexplore.ieee.org/document/8264768/>
- [21] S. Yang, B. He, Z. Wang, C. Xu, and F. Gao, "Whole-body real-time motion planning for multicopters," in *2021 IEEE International Conference on Robotics and Automation (ICRA)*. IEEE, pp. 9197–9203. [Online]. Available: <https://ieeexplore.ieee.org/document/9561526/>
- [22] H. Kim, H. Seo, J. Kim, and H. J. Kim, "Sampling-based motion planning for aerial pick-and-place."
- [23] C. Y. Son, T. Kim, S. Kim, and H. J. Kim, "Model predictive control of a multi-rotor with a slung load for avoiding obstacles," in *2017 14th International Conference on Ubiquitous Robots and Ambient Intelligence (URAI)*, 2017, pp. 232–237.
- [24] M. Neunert, C. de Crousaz, F. Furrer, M. Kamel, F. Farshidian, R. Siegwart, and J. Buchli, "Fast nonlinear model predictive control for unified trajectory optimization and tracking," in *2016 IEEE International Conference on Robotics and Automation (ICRA)*, 2016, pp. 1398–1404.
- [25] H. Seo, S. Kim, and H. J. Kim, "Locally optimal trajectory planning for aerial manipulation in constrained environments," in *2017 IEEE/RSJ International Conference on Intelligent Robots*

- and Systems (IROS)*. IEEE, pp. 1719–1724. [Online]. Available: <http://ieeexplore.ieee.org/document/8205984/>
- [26] M. Ryll, G. Muscio, F. Pierri, E. Cataldi, G. Antonelli, F. Caccavale, D. Bicego, and A. Franchi, “6d interaction control with aerial robots: The flying end-effector paradigm,” vol. 38, no. 9, pp. 1045–1062. [Online]. Available: <http://journals.sagepub.com/doi/10.1177/0278364919856694>
- [27] K. Bodie, M. Brunner, M. Pantic, S. Walsler, P. Pfandler, U. Angst, R. Siegwart, and J. Nieto, “Active interaction force control for contact-based inspection with a fully actuated aerial vehicle,” vol. 37, no. 3, pp. 709–722. [Online]. Available: <https://ieeexplore.ieee.org/document/9295362/>
- [28] H.-N. Nguyen, S. Park, J. Park, and D. Lee, “A novel robotic platform for aerial manipulation using quadrotors as rotating thrust generators,” vol. 34, no. 2, pp. 353–369. [Online]. Available: <http://ieeexplore.ieee.org/document/8294249/>
- [29] Z. Wang, X. Zhou, C. Xu, and F. Gao, “Geometrically constrained trajectory optimization for multicopters,” *IEEE Transactions on Robotics*, vol. 38, no. 5, pp. 3259–3278, 2022.
- [30] J. Ji, T. Yang, C. Xu, and F. Gao, “Real-time trajectory planning for aerial perching,” in *2022 IEEE/RSJ International Conference on Intelligent Robots and Systems (IROS)*, 2022, pp. 10 516–10 522.
- [31] H. Chen, B. Ye, X. Liang, W. Deng, and X. Lyu, “NDOB-based control of a UAV with delta-arm considering manipulator dynamics.”
- [32] D. Mellinger and V. Kumar, “Minimum snap trajectory generation and control for quadrotors,” in *2011 IEEE International Conference on Robotics and Automation*, 2011, pp. 2520–2525.
- [33] A. Codourey, “Dynamic modelling and mass matrix evaluation of the delta parallel robot for axes decoupling control,” in *Proceedings of the IEEE/RSJ International Conference on Intelligent Robots and Systems (IROS '96)*, vol. 3, 1996, pp. 1211–1218.
- [34] J. Welde and V. Kumar, “Coordinate-free dynamics and differential flatness of a class of 6dof aerial manipulators,” in *2020 IEEE International Conference on Robotics and Automation (ICRA)*. IEEE, pp. 4307–4313. [Online]. Available: <https://ieeexplore.ieee.org/document/9196705/>
- [35] Y. Ren, S. Liang, F. Zhu, G. Lu, and F. Zhang, “Online whole-body motion planning for quadrotor using multi-resolution search,” in *2023 IEEE International Conference on Robotics and Automation (ICRA)*. IEEE, pp. 1594–1600. [Online]. Available: <https://ieeexplore.ieee.org/document/10160767/>
- [36] S. Liu, M. Watterson, K. Mohta, K. Sun, S. Bhattacharya, C. J. Taylor, and V. Kumar, “Planning dynamically feasible trajectories for quadrotors using safe flight corridors in 3-d complex environments,” vol. 2, no. 3, pp. 1688–1695. [Online]. Available: <http://ieeexplore.ieee.org/document/7839930/>
- [37] Z. Han, Z. Wang, N. Pan, Y. Lin, C. Xu, and F. Gao, “Fast-racing: An open-source strong baseline for $\mathrm{SE}(3)$ planning in autonomous drone racing,” vol. 6, no. 4, pp. 8631–8638. [Online]. Available: <https://ieeexplore.ieee.org/document/9543598/>
- [38] Y. Gao, J. Ji, Q. Wang, R. Jin, Y. Lin, Z. Shang, Y. Cao, S. Shen, C. Xu, and F. Gao, “Adaptive tracking and perching for quadrotor in dynamic scenarios,” vol. 40, pp. 499–519. [Online]. Available: <https://ieeexplore.ieee.org/document/10328688/>